

# Large-Pore Mesoporous CeO<sub>2</sub>–ZrO<sub>2</sub> Solid Solutions with In-Pore Confined Pt Nanoparticles for Enhanced CO Oxidation

Xuanyu Yang, Xiaowei Cheng,\* Junhao Ma, Yidong Zou, Wei Luo,\* and Yonghui Deng\*

Active and stable catalysts are highly desired for converting harmful substances (e.g., CO, NO<sub>x</sub>) in exhaust gases of vehicles into safe gases at low exhaust temperatures. Here, a solvent evaporation–induced co-assembly process is employed to design ordered mesoporous Ce<sub>x</sub>Zr<sub>1–x</sub>O<sub>2</sub> (0 ≤ x ≤ 1) solid solutions by using high-molecular-weight poly(ethylene oxide)-*block*-polystyrene as the template. The obtained mesoporous Ce<sub>x</sub>Zr<sub>1–x</sub>O<sub>2</sub> possesses high surface area (60–100 m<sup>2</sup> g<sup>–1</sup>) and large pore size (12–15 nm), enabling its great capacity in stably immobilizing Pt nanoparticles (4.0 nm) without blocking pore channels. The obtained mesoporous Pt/Ce<sub>0.8</sub>Zr<sub>0.2</sub>O<sub>2</sub> catalyst exhibits superior CO oxidation activity with a very low T<sub>100</sub> value of 130 °C (temperature of 100% CO conversion) and excellent stability due to the rich lattice oxygen vacancies in the Ce<sub>0.8</sub>Zr<sub>0.2</sub>O<sub>2</sub> framework. The simulated catalytic evaluations of CO oxidation combined with various characterizations reveal that the intrinsic high surface oxygen mobility and well-interconnected pore structure of the mesoporous Pt/Ce<sub>0.8</sub>Zr<sub>0.2</sub>O<sub>2</sub> catalyst are responsible for the remarkable catalytic efficiency. Additionally, compared with mesoporous Pt/Ce<sub>x</sub>Zr<sub>1–x</sub>O<sub>2</sub>-s with small pore size (3.8 nm), ordered mesoporous Pt/Ce<sub>x</sub>Zr<sub>1–x</sub>O<sub>2</sub> not only facilitates the mass diffusion of reactants and products, but also provides abundant anchoring sites for Pt nanoparticles and numerous exposed catalytically active interfaces for efficient heterogeneous catalysis.

## 1. Introduction

Nowadays, severe effects of automobile exhaust gas on environment and human health, caused by the major harmful pollutants such as CO, NO<sub>x</sub>, hydrocarbons, and particulate matter,

Dr. X. Yang, Prof. X. Cheng, J. Ma, Y. Zou, Prof. Y. Deng  
Department of Chemistry  
State Key Laboratory of Molecular Engineering of Polymers  
Shanghai Key Laboratory of Molecular Catalysis and Innovative Materials  
iChEM

Fudan University  
Shanghai 200433, China  
E-mail: xwcheng@fudan.edu.cn; yhdeng@fudan.edu.cn

Prof. W. Luo  
State Key Laboratory for Modification of Chemical  
Fibers and Polymer Materials  
College of Materials Science and Engineering  
Donghua University  
Shanghai 201620, China  
E-mail: wluo@dhu.edu.cn

The ORCID identification number(s) for the author(s) of this article can be found under <https://doi.org/10.1002/smll.201903058>.

DOI: 10.1002/smll.201903058

have attracted increasing concerns. The catalytic converter in combustion engines is one of the most efficient methods to abate vehicle emission, in which CO catalytic oxidation to CO<sub>2</sub> is a key reaction.<sup>[1,2]</sup> Therefore, to meet increasingly strict emission standards, high-performance and stable catalysts in advanced engines are in urgent demand to work at the exhaust temperatures below 150 °C.<sup>[1]</sup> During the past decade, the platinum (Pt)-based catalysts have been widely explored for CO low-temperature oxidation.<sup>[2b]</sup> However, Pt nanoparticles containing zero-valent atoms tend to migrate on the support in oxidizing atmosphere and aggregate or sinter into large particles, resulting in loss of catalytic activity.<sup>[3]</sup> Therefore, considerable efforts have been made to rationally design the sinter-resistant catalysts with different nanostructures and high surface area, such as core–shell structure,<sup>[3]</sup> nanotube,<sup>[4]</sup> porous materials,<sup>[5]</sup> and so on. Besides, the metal oxide–metal interface can easily produce charges that help to enhance catalytic efficiency in CO oxidation,<sup>[5]</sup> so various metal oxides with redox properties, such as Co<sub>3</sub>O<sub>4</sub>,<sup>[5]</sup> TiO<sub>2</sub>,<sup>[6]</sup> FeO<sub>x</sub>,<sup>[7a]</sup> MnO<sub>2</sub>,<sup>[8]</sup> and CeO<sub>2</sub>,<sup>[1]</sup> have been explored as supporting matrix for Pt nanoparticles.

As a typical transition metal oxide, CeO<sub>2</sub> owns excellent oxygen storage capacity and facile interconversion between Ce<sup>3+</sup> and Ce<sup>4+</sup>, which has been regarded as one of the particularly promising candidates for loading Pt nanoparticles.<sup>[9]</sup> However, pure CeO<sub>2</sub> nanocrystals usually suffer several major drawbacks such as poor thermal stability and severe deactivation due to rapid sintering.<sup>[10]</sup> These problems can be well overcome by introducing foreign elements (e.g., Zr,<sup>[11]</sup> La,<sup>[12]</sup> and Pr<sup>[13]</sup>) into CeO<sub>2</sub> lattice to construct the so-called solid solutions, and they show increasing redox properties and catalytic performance in CO oxidation due to the significantly enhanced generation of lattice oxygen vacancies.<sup>[14]</sup> Particularly, CeO<sub>2</sub>–ZrO<sub>2</sub> (Ce<sub>x</sub>Zr<sub>1–x</sub>O<sub>2</sub>) solid solutions formed by introducing Zr<sup>4+</sup> in CeO<sub>2</sub> lattice possess distorted O<sup>2–</sup> sublattices and easy mobility of lattice oxygen from bulk phase to surface, which endows them with excellent thermal stability against high-temperature sintering and improved oxygen storage capacity.<sup>[15]</sup>

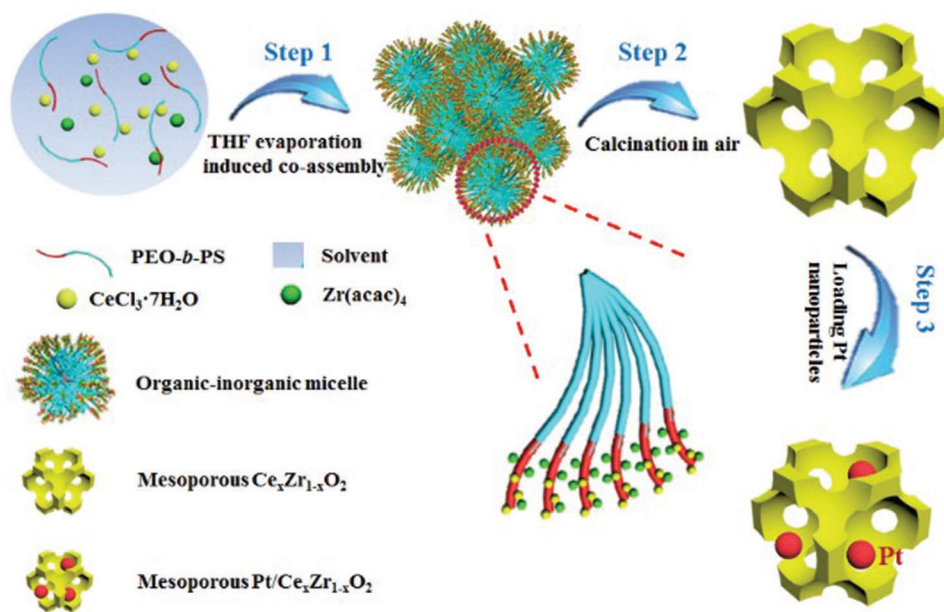
Ordered mesoporous metal oxides with high porosity and surface area have received great attention, because they not only provide enormous uniform pore channels beneficial to mass diffusion, but also offer huge accessible interface for

homogeneous loading and dispersion of active species such as Pt nanoparticles. These diverse features enable them to own great potential for applications in catalysis, adsorption and separation, energy storage, and chemical sensors.<sup>[15b,16]</sup> Although porous  $Ce_xZr_{1-x}O_2$  solid solutions have been reported previously by using different templates, including colloidal crystals,<sup>[13,14]</sup> amphiphilic cationic surfactant (cetyltrimethylammonium bromide),<sup>[17]</sup> and nonionic block copolymers (poly(ethylene oxide)-*b*-poly(propylene oxide)-*b*-poly(ethylene oxide))<sup>[18,19]</sup> and poly(ethylene-*co*-butylene)-*b*-poly(ethylene oxide)),<sup>[20]</sup> the obtained mesoporous  $Ce_xZr_{1-x}O_2$  materials still suffer the disadvantages of poor thermal stability (<500 °C), low crystallinity, and small mesopores (<10 nm), which are unfavorable to load metals or metal oxides in mesopores as active species for catalysis. To date, it still remains a great challenge to synthesize highly ordered mesoporous  $Ce_xZr_{1-x}O_2$  solid solutions with well-connected large pores (>10 nm) and fully crystalline framework, which are desirable to stably load Pt nanoparticles and improve catalytic efficiency for CO oxidation as well. In recent years, our group has succeeded in designing new amphiphilic block copolymer templates of poly(ethylene oxide)-*b*-polystyrene (PEO-*b*-PS), which have hydrophobic PS segments of high molecular weights and relatively higher thermodegradation temperatures than most reported copolymers. These novel templates were demonstrated to be powerful for synthesis of mesoporous metal oxides of single component, such as  $TiO_2$ ,<sup>[21]</sup>  $WO_3$ ,<sup>[22]</sup>  $Nb_2O_5$ ,<sup>[23]</sup> and  $Al_2O_3$ ,<sup>[24]</sup> with large mesopores, high crystallinity, and enhanced mass transport. They possessed high surface area with numerous exposed and accessible active sites, and thus showed advantages in creating rich metal oxide–metal interfaces for catalysis.<sup>[22b]</sup>

Herein, we report a solvent evaporation–induced co-assembly strategy to controllably synthesize highly ordered mesoporous  $Ce_xZr_{1-x}O_2$  ( $0 < x < 1$ ) solid solutions with large pores, highly crystalline pore walls, and tunable Ce/Zr molar ratios, using lab-made PEO-*b*-PS of high molecular weight as the template. After further loading ultrafine Pt nanoparticles ( $\approx 4.0$  nm), one of the obtained catalysts, mesoporous Pt/ $Ce_{0.8}Zr_{0.2}O_2$ , shows superior catalytic performance in CO oxidation with a low light-off temperature of 130 °C and long-term stability over 50 cycles compared with other mesoporous Pt/ $Ce_xZr_{1-x}O_2$  materials and the mesoporous Pt/ $Ce_{0.8}Zr_{0.2}O_2$ s with small pore size. The enhanced catalytic performance can be attributed to the intrinsic catalytic properties and the interconnected large-pore structures of mesoporous Pt/ $Ce_{0.8}Zr_{0.2}O_2$  catalyst, which promise the high surface oxygen mobility during the reaction and provide abundant catalytic interfaces, respectively. The results could give a great opportunity for large-pore mesoporous Pt/ $Ce_xZr_{1-x}O_2$  catalysts used as the commercial catalysts in catalytic convertor of advanced engines and other catalytic reactions.

## 2. Results and Discussion

**Scheme 1** illustrates the synthesis strategy of ordered mesoporous  $Ce_xZr_{1-x}O_2$  ( $0 < x < 1$ ) solid solutions and Pt/ $Ce_xZr_{1-x}O_2$  catalysts. Typically, the water-insoluble diblock copolymer of PEO-*b*-PS was dissolved in tetrahydrofuran, and then the solution was mixed with an ethanolic solution containing  $Zr(acac)_4$  and  $CeCl_3 \cdot 7H_2O$  to form the homogeneous solution. Because the hydrolyzed hydrophilic inorganic zirconium and cerium species can interact with the PEO segments



**Scheme 1.** The synthesis process of ordered mesoporous  $Ce_xZr_{1-x}O_2$  solid solutions and Pt/ $Ce_xZr_{1-x}O_2$  catalysts. Step 1: the spherical PEO-*b*-PS/inorganic sol composite micelles with PS blocks as the core and PEO segments as the shell were formed and packed into ordered fcc mesostructure with the evaporation of solvent. Step 2: ordered mesoporous  $Ce_xZr_{1-x}O_2$  ( $0 < x < 1$ ) solid solutions with large mesopores and tunable Ce/Zr ratios were obtained by calcination in air at 600 °C. Step 3: the functional Pt/ $Ce_xZr_{1-x}O_2$  catalysts were synthesized through in situ reduction of  $H_2PtCl_6$  aqueous solution containing  $Ce_xZr_{1-x}O_2$  powders by  $NaBH_4$ .

by hydrogen bonding,<sup>[18–20]</sup> during the solvent evaporation process, PEO-*b*-PS copolymers tend to form spherical composite micelles composed of hydrophobic PS blocks as the core and inorganic species associated PEO segments as the shell. The spherical composite micelles gradually pack into face-centered cubic (fcc) ordered mesostructures to achieve a minimum interface free energy (step 1). The as-formed inorganic-polymer composites were further calcined in air at 600 °C to remove the template and promote the crystallization of CeO<sub>2</sub>-ZrO<sub>2</sub> framework, and then the ordered mesoporous Ce<sub>x</sub>Zr<sub>1-x</sub>O<sub>2</sub> (0 < *x* < 1) solid solutions with large mesopores and tunable Ce/Zr ratios were obtained (step 2). For comparison, in this work mesoporous CeO<sub>2</sub>, Ce<sub>0.8</sub>Zr<sub>0.2</sub>O<sub>2</sub>, Ce<sub>0.5</sub>Zr<sub>0.5</sub>O<sub>2</sub>, Ce<sub>0.2</sub>Zr<sub>0.8</sub>O<sub>2</sub>, and ZrO<sub>2</sub> were synthesized and studied in detail. Finally, through in situ reduction of H<sub>2</sub>PtCl<sub>6</sub> · 6H<sub>2</sub>O aqueous solution by NaBH<sub>4</sub>, Pt nanoparticles were deposited within the pore channels of the ordered mesoporous Ce<sub>x</sub>Zr<sub>1-x</sub>O<sub>2</sub> solid solutions (step 3), and the Pt/Ce<sub>x</sub>Zr<sub>1-x</sub>O<sub>2</sub> materials were used as catalysts in CO low-temperature oxidation.

The wide-angle X-ray diffraction (XRD) pattern of pure mesoporous CeO<sub>2</sub> displays four well-resolved diffraction peaks (Figure 1A, e) indexed to (111), (200), (220), and (311) reflections of cubic fluorite-type structure (JCPDS Card No. 34-0394), respectively. With the introduction of zirconium of increasing contents from Ce<sub>0.8</sub>Zr<sub>0.2</sub>O<sub>2</sub> to Ce<sub>0.5</sub>Zr<sub>0.5</sub>O<sub>2</sub> and to Ce<sub>0.2</sub>Zr<sub>0.8</sub>O<sub>2</sub>, the obtained mesoporous Ce<sub>x</sub>Zr<sub>1-x</sub>O<sub>2</sub> materials exhibit peaks shifting to higher diffraction angles (Figure 1A, d–b). Such

phenomenon is attributed to the slight lattice shrinkage induced by partial replacement of Ce<sup>4+</sup> cations (0.97 Å) with smaller radius Zr<sup>4+</sup> cations (0.84 Å),<sup>[14,25]</sup> which indicates the uniform formation of CeO<sub>2</sub>-ZrO<sub>2</sub> solid solutions. The pure mesoporous ZrO<sub>2</sub> shows well-resolved diffraction peaks in range of 10–70°/2θ (Figure 1A, a), corresponding to the typical tetragonal phase of ZrO<sub>2</sub> (JCPDS Card No. 50-1089). It should be mentioned that, in comparison with pure mesoporous CeO<sub>2</sub> and ZrO<sub>2</sub> with relatively sharp diffraction peaks (Figure 1A, e and a), the samples of mesoporous Ce<sub>0.8</sub>Zr<sub>0.2</sub>O<sub>2</sub>, Ce<sub>0.5</sub>Zr<sub>0.5</sub>O<sub>2</sub>, and Ce<sub>0.2</sub>Zr<sub>0.8</sub>O<sub>2</sub> exhibit broadened peaks (Figure 1A, d–b), implying the formation of smaller Ce<sub>x</sub>Zr<sub>1-x</sub>O<sub>2</sub> crystallites in the framework. This result clearly indicates that the cohydrolysis of cerium with zirconium precursors and their co-assembly with block copolymers tend to form Ce<sub>x</sub>Zr<sub>1-x</sub>O<sub>2</sub> crystallites at nanoscale with enhanced thermal stability.<sup>[10a]</sup> Ce<sub>x</sub>Zr<sub>1-x</sub>O<sub>2</sub> solid solutions have three stable phases, i.e., monoclinic, tetragonal, and cubic,<sup>[26]</sup> but it is difficult to identify their crystallographic structure simply according to the broadened diffraction peaks in XRD patterns. Raman spectroscopy is very sensitive to recognize both M–O (M represents metal) bond arrangement and lattice defects, which can be used to further determine the exact phases of our mesoporous Ce<sub>x</sub>Zr<sub>1-x</sub>O<sub>2</sub> samples. Generally, there is only one F<sub>2g</sub> Raman active mode centered at around 470 cm<sup>-1</sup> in cubic fluorite CeO<sub>2</sub>, while tetragonal ZrO<sub>2</sub> exhibits six Raman active modes (A<sub>1g</sub> + 2B<sub>1g</sub> + 3E<sub>g</sub>).<sup>[14,19]</sup> In this study, the samples of mesoporous CeO<sub>2</sub>, Ce<sub>0.8</sub>Zr<sub>0.2</sub>O<sub>2</sub>, and Ce<sub>0.5</sub>Zr<sub>0.5</sub>O<sub>2</sub> show one

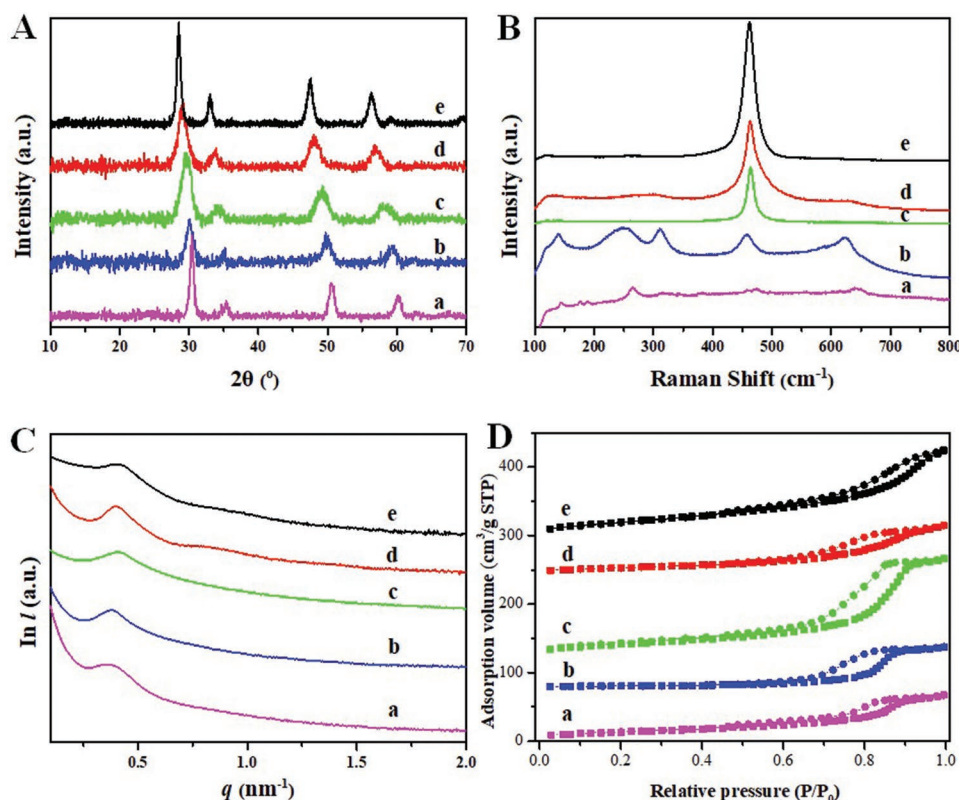


**Figure 1.** A) XRD patterns, B) Raman spectra, C) SAXS patterns, and D) N<sub>2</sub> sorption isotherms of the ordered mesoporous Ce<sub>x</sub>Zr<sub>1-x</sub>O<sub>2</sub> samples (0 ≤ *x* ≤ 1) (a, ZrO<sub>2</sub>; b, Ce<sub>0.2</sub>Zr<sub>0.8</sub>O<sub>2</sub>; c, Ce<sub>0.5</sub>Zr<sub>0.5</sub>O<sub>2</sub>; d, Ce<sub>0.8</sub>Zr<sub>0.2</sub>O<sub>2</sub>; e, CeO<sub>2</sub>). The sorption isotherms are vertically offset by 50, 100, 150, and 200 cm<sup>3</sup> g<sup>-1</sup> from (b) to (e), respectively, for clarity. STP: standard temperature and pressure.

strong Raman band at  $470\text{ cm}^{-1}$ , whose intensity diminishes with the increase of zirconium content (Figure 1B, e–c). It confirms their structure of cubic fluorite phase, in good agreement with the corresponding XRD patterns (Figure 1A, e–c). For the zirconium-rich samples (Figure 1B, b and a), the appearance of six Raman bands located at 150, 268, 320, 465, 560, and  $630\text{ cm}^{-1}$  illustrates the formation of  $\text{Ce}_{0.2}\text{Zr}_{0.8}\text{O}_2$  solid solutions or  $\text{ZrO}_2$  with stable tetragonal phase.

Small-angle X-ray scattering (SAXS) patterns of all  $\text{Ce}_x\text{Zr}_{1-x}\text{O}_2$  samples exhibit three well-resolved scattering peaks (Figure 1C), which can be exactly indexed to the 111, 311, and 400 reflections of the ordered fcc mesostructure with the space group of  $Fm\bar{3}m$ .<sup>[24]</sup> Compared to the mesoporous  $\text{Ce}_x\text{Zr}_{1-x}\text{O}_2$  solid solutions and  $\text{ZrO}_2$  samples (Figure 1C, d–a), the scattering peaks of mesoporous  $\text{CeO}_2$  shift to higher  $q$  values (Figure 1C, e). The unit cell parameter is calculated to be 27.2 nm, smaller than that of the mesoporous zirconium-containing samples (Table S1, Supporting Information), implying the mesoporous  $\text{CeO}_2$  underwent a distinct structural shrinkage and large grains were formed during high-temperature crystallization because of its relatively poor thermal stability. These results further confirm that the introduction of zirconium in mesoporous  $\text{CeO}_2$  can significantly improve the thermal stability by preventing the structural shrinkage and generation of large grains, in good accordance with XRD patterns. Nitrogen adsorption–desorption isotherms of mesoporous  $\text{Ce}_x\text{Zr}_{1-x}\text{O}_2$  samples ( $0 \leq x \leq 1$ ) show the typical type-IV curves with  $\text{H}_1$ -type hysteresis loops (Figure 1D). The sharp capillary condensation step occurs in the relative pressure ( $P/P_0$ ) range of 0.80–0.90, implying the formation of large uniform mesopores in each sample. Based on the Barrett–Joyner–Halenda model, the average pore sizes derived from the adsorption branch of the isotherms are calculated to be 10.6, 12.9, 13.3, 14.9, and 15.1 nm for mesoporous  $\text{CeO}_2$ ,  $\text{Ce}_{0.8}\text{Zr}_{0.2}\text{O}_2$ ,  $\text{Ce}_{0.5}\text{Zr}_{0.5}\text{O}_2$ ,  $\text{Ce}_{0.2}\text{Zr}_{0.8}\text{O}_2$ , and  $\text{ZrO}_2$ , respectively (Figure S1 and Table S1, Supporting Information). It provides an additional evidence that doping zirconium in mesoporous  $\text{CeO}_2$  can effectively prevent the framework shrinkage during calcination and benefit the formation of larger unit cells and mesopores, in good consistence with SAXS results. The Brunauer–Emmett–Teller (BET) surface area and pore volume of mesoporous  $\text{Ce}_{0.8}\text{Zr}_{0.2}\text{O}_2$ ,  $\text{Ce}_{0.5}\text{Zr}_{0.5}\text{O}_2$ , and  $\text{Ce}_{0.2}\text{Zr}_{0.8}\text{O}_2$  solid solutions are in the range of  $65.8\text{--}73.7\text{ m}^2\text{ g}^{-1}$  and  $0.121\text{--}0.136\text{ cm}^3\text{ g}^{-1}$  (Table S1, Supporting Information), respectively, which are noticeably high for mesoporous metal oxides considering the high density of  $\text{Ce}_x\text{Zr}_{1-x}\text{O}_2$  solid solutions and their large pore size ( $>10\text{ nm}$ ). The mesoporous  $\text{CeO}_2$  has a BET surface area of  $48.7\text{ m}^2\text{ g}^{-1}$  and a pore volume of  $0.112\text{ cm}^3\text{ g}^{-1}$ , lower than those of mesoporous zirconium-containing samples, also proving that  $\text{Ce}_x\text{Zr}_{1-x}\text{O}_2$  solid solutions can improve the framework thermal stability, and then prohibit the formation of large grains.

Field-emission scanning electron microscope (FESEM) characterizations (Figure 2A,B) from both the surface and the cross-sections of  $\text{Ce}_{0.8}\text{Zr}_{0.2}\text{O}_2$  solid solutions exhibit the highly ordered and well-interconnected mesostructure over a large domain. Transmission electron microscopy (TEM) images taken along [100], [110], and [211] directions (Figure 2C–E) further confirm the ordered fcc mesostructure ( $Fm\bar{3}m$  symmetry) with large pore size and high degree of periodicity over large domains. The visible crystal lattice of  $\text{Ce}_{0.8}\text{Zr}_{0.2}\text{O}_2$  was observed from the

high-resolution TEM image (Figure 2F), and the  $d$ -spacing of 0.309 nm can be well indexed to the (111) lattice plane. The corresponding selected area electron diffraction (SAED) pattern (Figure 2F, inset) with clear spotted diffraction rings further confirms the polycrystalline walls of mesoporous  $\text{Ce}_{0.8}\text{Zr}_{0.2}\text{O}_2$ . The other samples of  $\text{CeO}_2$ ,  $\text{Ce}_{0.5}\text{Zr}_{0.5}\text{O}_2$ ,  $\text{Ce}_{0.2}\text{Zr}_{0.8}\text{O}_2$ , and  $\text{ZrO}_2$  also possess highly ordered fcc mesoporous structure with uniform spherical mesopores and highly crystalline walls (Figures S2–S5, Supporting Information). As zirconium content increases in mesoporous  $\text{Ce}_x\text{Zr}_{1-x}\text{O}_2$ , the  $d$ -spacing of (111) lattice plane gradually decreases from 0.312 to 0.294 nm (Table S1, Supporting Information), showing the lattice shrinkage, which agrees well with XRD measurement results.

Because the crystalline mesoporous  $\text{Ce}_x\text{Zr}_{1-x}\text{O}_2$  solid solutions present the well-connected porous structures with high surface area, large pores, intrinsic reducibility, and high oxygen storage capacity, they can provide the enhanced target–receptor interface, making them an ideal carrier for supported catalysts in various heterogeneous catalytic reactions. In this study, mesoporous Pt/ $\text{Ce}_x\text{Zr}_{1-x}\text{O}_2$  samples were obtained through decorating Pt nanoparticles, which were further utilized as the catalysts for CO oxidation, a crucial reaction in catalytic converter of automobile exhaust. A series of mesoporous Pt/ $\text{Ce}_x\text{Zr}_{1-x}\text{O}_2$  samples were synthesized by impregnating the mesoporous  $\text{Ce}_x\text{Zr}_{1-x}\text{O}_2$  samples (e.g.,  $\text{Ce}_{0.8}\text{Zr}_{0.2}\text{O}_2$ ) with  $\text{H}_2\text{PtCl}_6$  solution followed by subsequent in situ reduction in  $\text{NaBH}_4$  solution.<sup>[27]</sup> Their surface area, pore volumes, and pore sizes slightly decrease due to the deposition of Pt nanoparticles in the mesopores (Table S1, Supporting Information). The mesoporous Pt/ $\text{Ce}_{0.8}\text{Zr}_{0.2}\text{O}_2$  sample with about 0.4 wt% Pt loading measured by inductively coupled plasma (ICP) (Table S2, Supporting Information) exhibits the same XRD pattern as the parent mesoporous  $\text{Ce}_{0.8}\text{Zr}_{0.2}\text{O}_2$ , and no signal about Pt nanoparticles is observed in the pattern (Figure S6, Supporting Information). High-angle annular dark-field scanning transmission electron microscopy (HAADF-STEM) image of Pt/ $\text{Ce}_{0.8}\text{Zr}_{0.2}\text{O}_2$  (Figure 3A) confirms the ordered mesoporous structure and homogeneous dispersion of ultrafine Pt nanoparticles in size of around 4.0 nm. The corresponding energy-dispersive X-ray (EDX) element mappings (Figure 3C–F) also show the uniform distributions of O, Ce, Zr, and Pt elements in mesoporous Pt/ $\text{Ce}_{0.8}\text{Zr}_{0.2}\text{O}_2$ . The Pt loading measured by energy-dispersive spectrometer (EDS; Table S2, Supporting Information) is 0.48 wt%, which is quite close to the ICP result. The combined TEM images with different rotation angles (Figure S15, Supporting Information),  $\text{N}_2$  adsorption, EDX mapping, and EDS results suggest that ultrafine Pt nanoparticles were uniformly dispersed within the crystalline mesoporous  $\text{Ce}_{0.8}\text{Zr}_{0.2}\text{O}_2$  matrix.

In order to study the catalytic performance of our mesoporous Pt/ $\text{Ce}_x\text{Zr}_{1-x}\text{O}_2$  materials in CO oxidation, the gas mixture of 1 vol% CO, 21 vol%  $\text{O}_2$ , and 78 vol%  $\text{N}_2$  was prepared and used as the reaction atmosphere.<sup>[1]</sup> The catalytic activities of the mesoporous Pt/ $\text{Ce}_x\text{Zr}_{1-x}\text{O}_2$  catalysts and their parent  $\text{Ce}_x\text{Zr}_{1-x}\text{O}_2$  matrix for CO oxidation are summarized in Figure 4 and Figure S7 (Supporting Information), respectively. The pure mesoporous  $\text{CeO}_2$  exhibits the light-off temperature (temperature of 100% CO conversion,  $T_{100}$  value) as high as  $403\text{ }^\circ\text{C}$  (Table S3, Supporting Information), and this value increases to  $470\text{ }^\circ\text{C}$  for mesoporous

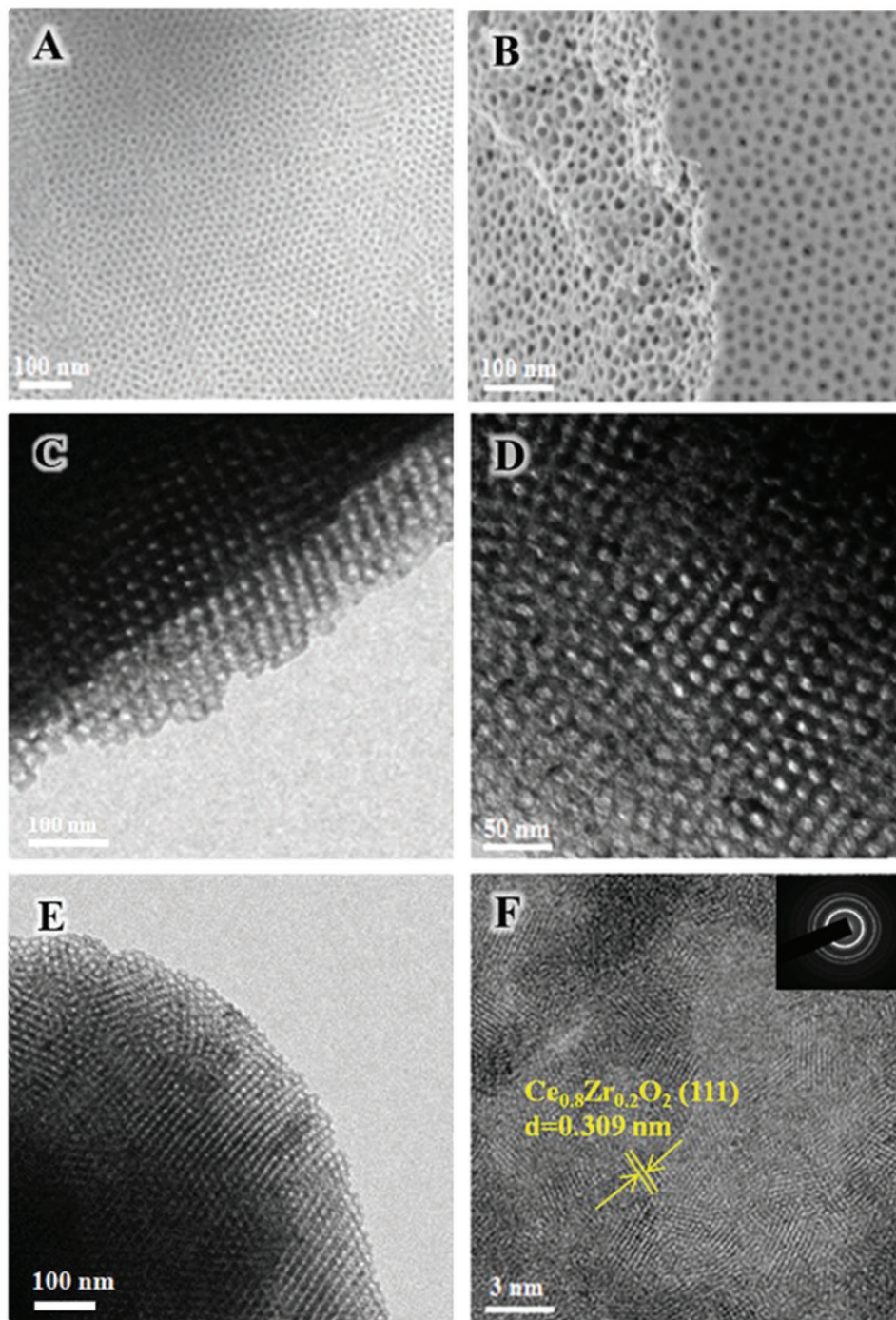


**Figure 2.** FESEM images of the ordered mesoporous  $\text{Ce}_{0.8}\text{Zr}_{0.2}\text{O}_2$ : A) surface and B) cross-section; and their TEM images taken along the directions of C) [100], D) [110], and E) [211]. F) High-resolution TEM image; the inset in the panel is the corresponding SAED pattern.

$\text{Ce}_{0.8}\text{Zr}_{0.2}\text{O}_2$  and to 582 °C for mesoporous  $\text{Ce}_{0.5}\text{Zr}_{0.5}\text{O}_2$ . Such lower catalytic activity of  $\text{Ce}_{0.8}\text{Zr}_{0.2}\text{O}_2$  and  $\text{Ce}_{0.5}\text{Zr}_{0.5}\text{O}_2$  in CO oxidation is mainly due to their lower content of catalytically active cerium species and weaker CO adsorbability. After loading about 0.4 wt% Pt nanoparticles, all the mesoporous Pt/ $\text{Ce}_x\text{Zr}_{1-x}\text{O}_2$  catalysts exhibit significantly improved low-temperature reactivity with  $T_{100}$  values lower than 200 °C (Figure 4A). Compared to mesoporous  $\text{CeO}_2$ , the onset temperature and  $T_{100}$  value on

mesoporous Pt/ $\text{CeO}_2$  are lowered to 120 and 150 °C, respectively. Noticeably, the mesoporous Pt/ $\text{Ce}_{0.8}\text{Zr}_{0.2}\text{O}_2$  exhibits better catalytic performance than mesoporous Pt/ $\text{CeO}_2$ , with the onset temperature of 100 °C and  $T_{100}$  value of 130 °C. The mesoporous Pt/ $\text{Ce}_{0.5}\text{Zr}_{0.5}\text{O}_2$  shows the comparable catalytic reactivity ( $T_{100} = 153$  °C) with mesoporous Pt/ $\text{CeO}_2$ , while as zirconium content further increases,  $T_{100}$  values increase to 170 and 198 °C for mesoporous Pt/ $\text{Ce}_{0.2}\text{Zr}_{0.8}\text{O}_2$  and Pt/ $\text{ZrO}_2$ , respectively. The

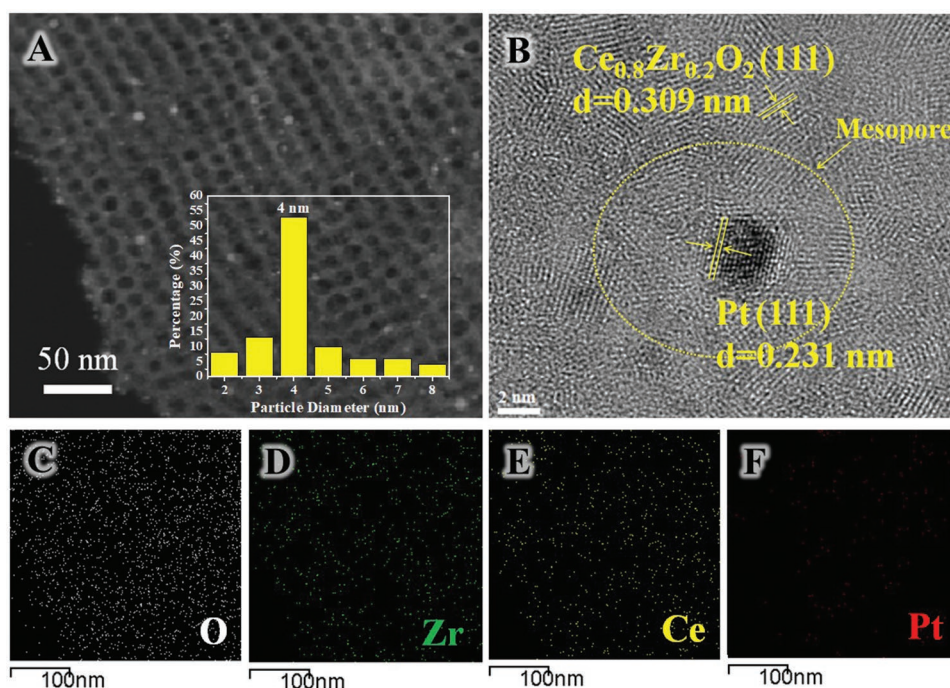


**Figure 3.** A) HAADF-STEM image, B) high-resolution TEM image, and energy-dispersive X-ray element mapping of C) O, D) Zr, E) Ce, and F) Pt elements in the ordered mesoporous Pt/Ce<sub>0.8</sub>Zr<sub>0.2</sub>O<sub>2</sub>; the inset in panel (A) is the size distribution of Pt nanoparticles.

Zr-content-dependent catalytic performance can be explained by considering the porosity and oxygen vacancies of Ce<sub>x</sub>Zr<sub>1-x</sub>O<sub>2</sub> solid solutions. On one hand, the partial replacement of Ce<sup>4+</sup> cations with Zr<sup>4+</sup> cations prevents the formation of large grains; thus, the Ce<sub>x</sub>Zr<sub>1-x</sub>O<sub>2</sub> catalyst exhibits much higher surface area and larger pore volume with more exposed active sites and enhanced mass diffusion. On the other hand, zirconium introduced into CeO<sub>2</sub> lattice with proper content (Zr/Ce < 0.2) can promote the formation of surface oxygen vacancies, proved by X-ray photoelectron spectroscopy (XPS) spectra in the following section, which are beneficial for the enhancement of catalytic efficiency. However, when too many Zr atoms entered the lattice (Zr/Ce > 0.5), the Ce content in the solid solutions decreased

dramatically, which led to a low concentration of active cerium species and inferior catalytic performance as well. To evaluate the durability of the best catalyst of mesoporous Pt/Ce<sub>0.8</sub>Zr<sub>0.2</sub>O<sub>2</sub>, the dynamic continuous CO conversion test was performed at 160 °C for 72 h with the gas hourly space velocity of 60 000 mL g<sup>-1</sup> h<sup>-1</sup>, and the results show that 100% CO conversion can be maintained during the whole period (Figure S7, Supporting Information). In addition, the recycling experiment running at 20–200 °C indicates that the mesoporous Pt/Ce<sub>0.8</sub>Zr<sub>0.2</sub>O<sub>2</sub> catalyst has a stable performance with T<sub>100</sub> value remaining at around 130 °C even after 50 cycles (Figure 4B). In order to investigate the effect of pore size on catalytic performance, mesoporous Pt/Ce<sub>0.8</sub>Zr<sub>0.2</sub>O<sub>2</sub>-s with smaller pores of 3.8 nm was synthesized by

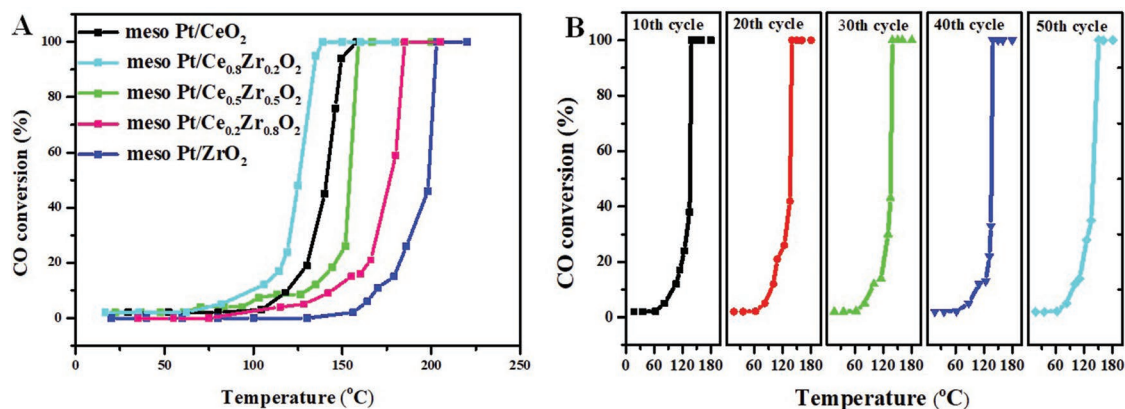


**Figure 4.** A) Light-off curves of CO oxidation on the catalysts of ordered mesoporous Pt/Ce<sub>x</sub>Zr<sub>1-x</sub>O<sub>2</sub> (0 ≤ x ≤ 1). B) CO conversion from 20 to 200 °C with 1st to 50th cycles by using the catalyst of ordered mesoporous Pt/Ce<sub>0.8</sub>Zr<sub>0.2</sub>O<sub>2</sub>. [CO] = 1 vol%, [O<sub>2</sub>] = 21 vol%, and balanced with N<sub>2</sub> (78 vol%) at a gas hourly space velocity of 60 000 mL g<sup>-1</sup> h<sup>-1</sup>. Temperature ramp: 1 °C min<sup>-1</sup>; pressure: 1 atm.

using Pluronic P123 as a template for comparison. Its light-off curve of CO oxidation shows  $T_{100}$  value at 150 °C (Figure S8 and Table S4, Supporting Information), higher than 130 °C for Pt/Ce<sub>0.8</sub>Zr<sub>0.2</sub>O<sub>2</sub> with a large pore size of 12.3 nm. In addition, we plot an Arrhenius profile, and give the pre-exponential factors ( $\Gamma$ ) of the reaction to estimate the number of possible active centers.<sup>[28a]</sup> The  $\Gamma$  value of Pt/Ce<sub>0.8</sub>Zr<sub>0.2</sub>O<sub>2</sub> ( $\approx 1.5 \times 10^5$ ) is much larger than that of Pt/Ce<sub>0.8</sub>Zr<sub>0.2</sub>O<sub>2-s</sub> ( $\approx 6.9 \times 10^4$ ), implying that the Pt/Ce<sub>0.8</sub>Zr<sub>0.2</sub>O<sub>2</sub> has more available active sites for CO oxidation than Pt/Ce<sub>0.8</sub>Zr<sub>0.2</sub>O<sub>2-s</sub> (Figure S9 and Table S4, Supporting Information). Despite the fact that the values of apparent activation energy ( $E_a$ ) of Pt/Ce<sub>0.8</sub>Zr<sub>0.2</sub>O<sub>2</sub> and Pt/Ce<sub>0.8</sub>Zr<sub>0.2</sub>O<sub>2-s</sub> are very close, the turnover frequency of Pt/Ce<sub>0.8</sub>Zr<sub>0.2</sub>O<sub>2</sub> is nearly twice that of Pt/Ce<sub>0.8</sub>Zr<sub>0.2</sub>O<sub>2-s</sub>. The results indicate that the mesoporous Pt/Ce<sub>0.8</sub>Zr<sub>0.2</sub>O<sub>2</sub> with large pore size and interconnected pore structure possesses more available anchoring sites for Pt nanoparticles within the ordered channels, thus providing abundant catalytic interfaces. However, much smaller pore size (3.8 nm) of Pt/Ce<sub>0.8</sub>Zr<sub>0.2</sub>O<sub>2-s</sub> is adverse to load Pt nanoparticles ( $\approx 4$  nm) in the pore channels, resulting in poor dispersion of Pt nanoparticles in the matrix surface. It is clearly demonstrated that much larger Pt nanoparticles ( $\approx 10$  nm) are formed on the surface of mesoporous Ce<sub>0.8</sub>Zr<sub>0.2</sub>O<sub>2-s</sub>, which are much larger than the pore size of Ce<sub>0.8</sub>Zr<sub>0.2</sub>O<sub>2-s</sub> (Figure S10, Supporting Information). Although Pt loading amount of Pt/Ce<sub>0.8</sub>Zr<sub>0.2</sub>O<sub>2-s</sub> is approximately the same as that of Pt/Ce<sub>0.8</sub>Zr<sub>0.2</sub>O<sub>2</sub>, the Pt nanoparticles are hardly dispersed inside the bulk mesostructure framework, and they are mainly anchored on the surface of matrix, resulting in fewer catalytic interfaces and poorer dispersion of Pt nanoparticles. In addition, much smaller Pt nanoparticles ( $\approx 4$  nm) facilitate CO oxidation compared with larger ones ( $\approx 10$  nm) due to more interfacial Pt atoms on the metal oxide–metal interfaces.<sup>[28b]</sup> Hence, the large-pore mesoporous Pt/Ce<sub>0.8</sub>Zr<sub>0.2</sub>O<sub>2</sub> exhibits much higher catalytic activity than the corresponding mesoporous Pt/Ce<sub>0.8</sub>Zr<sub>0.2</sub>O<sub>2-s</sub> with small pore size.

H<sub>2</sub> temperature-programmed reduction (TPR) measurement was conducted to assess the intrinsic reducibility of the obtained samples, and the hydrogen consumption profiles as a function of temperature were displayed in Figure S11 (Supporting Information). The pristine mesoporous CeO<sub>2</sub> exhibits two reduction peaks at around 550 and 850 °C, ascribed to the surface and bulk reduction of Ce<sup>4+</sup>, respectively.<sup>[10a]</sup> The H<sub>2</sub>-TPR profile of mesoporous Ce<sub>0.8</sub>Zr<sub>0.2</sub>O<sub>2</sub> solid solutions also presents two reduction peaks centered at 450 and 650 °C, much lower than those of mesoporous CeO<sub>2</sub>, which is mainly due to the increased mobility of lattice oxygen from bulk to surface after introduction of Zr<sup>4+</sup> into CeO<sub>2</sub> lattice.<sup>[29]</sup> Furthermore, the supported Pt nanoparticles can dramatically enhance the reduction capacity of the surface oxygen in CeO<sub>2</sub> or Ce<sub>x</sub>Zr<sub>1-x</sub>O<sub>2</sub> solid solutions.<sup>[10c]</sup> Therefore, the mesoporous Pt/Ce<sub>0.8</sub>Zr<sub>0.2</sub>O<sub>2</sub> catalyst displays reduction peaks at much lower temperatures of 350 and 600 °C and shows much higher H<sub>2</sub> consumption than the parent mesoporous Ce<sub>0.8</sub>Zr<sub>0.2</sub>O<sub>2</sub>.<sup>[10c]</sup> This phenomenon can be attributed to the dissociated H<sub>2</sub> on Pt surfaces and the formed hydrogen spillover onto the vicinity of metal oxide support, which can promote the reduction of metal oxide support at low temperature.<sup>[10,29,30]</sup> Similar results were also observed in other Pt supported catalysts (Figure S11B, Supporting Information). It can be seen that the mesoporous Pt/Ce<sub>0.8</sub>Zr<sub>0.2</sub>O<sub>2</sub>

presents the lowest reduction temperatures (350 and 600 °C) and the highest H<sub>2</sub> consumption (0.87 mmol g<sup>-1</sup>; Table S3, Supporting Information), in good agreement with its best catalytic activity in CO oxidation.

In addition, XPS was performed to acquire more detailed information about surface chemical compositions and element valence states in our mesoporous samples. The XPS spectra of Pt 4f, Ce 3d, and O 1s of mesoporous Pt/Ce<sub>0.8</sub>Zr<sub>0.2</sub>O<sub>2</sub> and Pt/CeO<sub>2</sub> catalysts are shown in Figure 5, and their corresponding element compositions calculated by the normalized peak areas are listed in Table S3 (Supporting Information). As shown in Figure 5A,D, the fitted binding energy peaks at 70.8 and 74.1 eV can be assigned to Pt<sup>0</sup> 4f<sub>7/2</sub> and Pt<sup>0</sup> 4f<sub>5/2</sub> of metallic Pt, while the signals at 72.7 and 76.0 eV are associated with Pt<sup>2+</sup> 4f<sub>7/2</sub> and Pt<sup>2+</sup> 4f<sub>5/2</sub> of cationic Pt<sup>2+</sup>, respectively.<sup>[27,30a]</sup> Both metallic Pt and cationic Pt<sup>2+</sup> species are present in mesoporous Pt/Ce<sub>0.8</sub>Zr<sub>0.2</sub>O<sub>2</sub> and Pt/CeO<sub>2</sub> samples, indicating that H<sub>2</sub>PtCl<sub>6</sub> was not fully reduced by NaBH<sub>4</sub> or metallic Pt was partially oxidized by oxygen during preparation. The Pt<sup>2+</sup>/Pt<sup>0</sup> atomic ratios calculated by the normalized peak areas of Pt 4f are 0.29 for mesoporous Pt/Ce<sub>0.8</sub>Zr<sub>0.2</sub>O<sub>2</sub> and 1.02 for mesoporous Pt/CeO<sub>2</sub>, demonstrating the quite different electronic environment of Pt species over the two mesoporous matrices due to the strong metal–support interaction effect.<sup>[30a]</sup> This result also indicates that metallic Pt species are the major form in mesoporous Pt/Ce<sub>0.8</sub>Zr<sub>0.2</sub>O<sub>2</sub> catalyst, which exhibit superior activity toward CO oxidation.<sup>[2b]</sup> The valence state of Ce in mesoporous Pt/Ce<sub>x</sub>Zr<sub>1-x</sub>O<sub>2</sub> and mesoporous Pt/CeO<sub>2</sub> samples can be obtained by analyzing the Ce 3d XPS spectra (Figure 5B,E). The peaks labeled as v<sub>1</sub>, v<sub>2</sub>, v<sub>3</sub> (3d<sub>5/2</sub>) and u<sub>1</sub>, u<sub>2</sub>, u<sub>3</sub> (3d<sub>3/2</sub>) are assigned to Ce<sup>4+</sup> 3d, while the peaks labeled as v<sub>1</sub> (3d<sub>5/2</sub>) and u<sub>1</sub> (3d<sub>3/2</sub>) are characteristic of Ce<sup>3+</sup> 3d.<sup>[27]</sup> These results indicate the coexistence of trivalent and tetravalent cerium species in both the pristine mesoporous Ce<sub>0.8</sub>Zr<sub>0.2</sub>O<sub>2</sub> and CeO<sub>2</sub> (Figure S12A,C, Supporting Information) and their Pt-loaded samples (Figure 5B,E, Supporting Information). The atomic ratio of Ce<sup>3+</sup>/(Ce<sup>3+</sup> + Ce<sup>4+</sup>) in all samples was calculated to be around 0.2 (Table S3, Supporting Information), implying that the introduction of zirconium and loading Pt nanoparticles produce a negligible effect on the valence states of Ce species. The XPS spectra of O 1s were used to identify the oxygen valence states in the samples (Figure 5C,F). The broad peaks could be fitted into two components at higher binding energy of 533–535 eV and lower binding energy of 530–532 eV, attributed to the surface chemisorbed oxygen (denoted as O<sup>α</sup>) and lattice O<sup>2-</sup> species (denoted as O<sup>β</sup>), respectively.<sup>[10a]</sup> The content of surface O<sup>α</sup> from calculation of O<sup>α</sup>/(O<sup>α</sup> + O<sup>β</sup>) on mesoporous CeO<sub>2</sub>, Ce<sub>0.8</sub>Zr<sub>0.2</sub>O<sub>2</sub>, Pt/CeO<sub>2</sub>, and Pt/Ce<sub>0.8</sub>Zr<sub>0.2</sub>O<sub>2</sub> is 0.16, 0.27, 0.26, and 0.32 (Table S3, Supporting Information), respectively, revealing that both zirconium doping and platinum loading could promote the surface oxygen production with the increase of oxygen vacancies. Actually, surface O<sup>α</sup> species show higher mobility during catalytic reactions, and the fast diffusion of oxygen adspecies endows the mesoporous Pt/Ce<sub>0.8</sub>Zr<sub>0.2</sub>O<sub>2</sub> with high catalytic efficiency at low temperature, resulting in its enhanced catalytic activity in CO oxidation.

In order to further investigate the mechanistic comprehension of the enhanced low-temperature CO oxidation reactivity of mesoporous Pt/Ce<sub>0.8</sub>Zr<sub>0.2</sub>O<sub>2</sub>, in situ CO diffuse reflectance infrared Fourier transform spectroscopy (DRIFTS) was carried

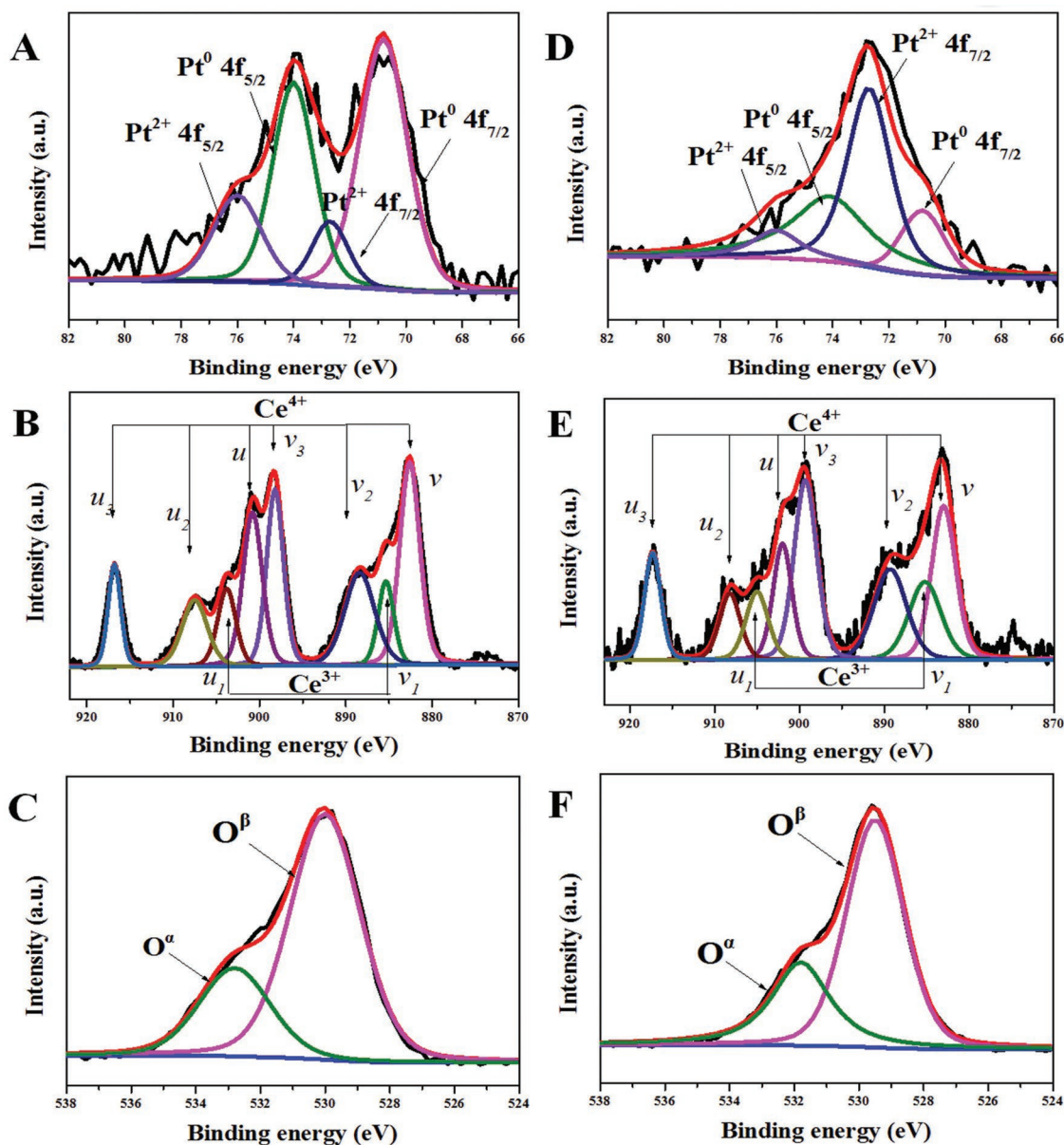


**Figure 5.** A) Pt 4f, B) Ce 3d, and C) O 1s XPS spectra of ordered mesoporous Pt/Ce<sub>0.8</sub>Zr<sub>0.2</sub>O<sub>2</sub>. D) Pt 4f, E) Ce 3d, and F) O 1s XPS spectra of ordered mesoporous Pt/CeO<sub>2</sub>.

out on mesoporous Pt/Ce<sub>0.8</sub>Zr<sub>0.2</sub>O<sub>2</sub> and Pt/CeO<sub>2</sub> for comparison (Figure 6). The isolated peak at around 1825 cm<sup>-1</sup> is assigned to the bridge bonded CO on Pt (Figure 6A,C), which is considered as a characteristic of Pt nanoparticles in both samples.<sup>[12a]</sup> The broad peaks in the range of 1950–2150 cm<sup>-1</sup> can be well resolved into two components centered at 2057 and 2089 cm<sup>-1</sup>, respectively. The shoulder peak at about 2057 cm<sup>-1</sup> is attributed to CO molecules linearly adsorbed on metallic Pt nanoparticles, and the narrow peak at 2089 cm<sup>-1</sup> is due to the IR absorption of CO on ionic Pt,<sup>[2b,d,12a]</sup> further confirming the coexistence of metallic and cationic Pt species in our Pt-loading mesoporous catalysts. As reported earlier, only the CO molecules adsorbed on metallic Pt nanoparticles can be oxidized and then desorbed as CO<sub>2</sub> from the adsorption sites at low reaction temperature.<sup>[2b]</sup>

However, CO on cationic Pt is not reactive at low temperature, which becomes more active only at higher temperature.<sup>[2d]</sup> Through calculating the integral area of the two resolved DRIFTS bands, the fraction of reactive CO molecules adsorbed on metallic Pt nanoparticles in mesoporous Pt/Ce<sub>0.8</sub>Zr<sub>0.2</sub>O<sub>2</sub> is 0.63, much higher than 0.48 in mesoporous Pt/CeO<sub>2</sub>, mainly because of the synergistic effects between Pt nanoparticles and Ce<sub>0.8</sub>Zr<sub>0.2</sub>O<sub>2</sub> solid solution matrix with more surface defect sites.<sup>[31,32]</sup> The results are quite consistent with Pt 4f XPS analysis, and the superior activity of mesoporous Pt/Ce<sub>0.8</sub>Zr<sub>0.2</sub>O<sub>2</sub> for CO oxidation in comparison with mesoporous Pt/CeO<sub>2</sub>.

It is widely accepted that CO oxidation over Pt/CeO<sub>2</sub> catalysts follows the Mars–van Krevelen reaction mechanism, namely, the CO molecules bonded on Pt are oxidized by the surface

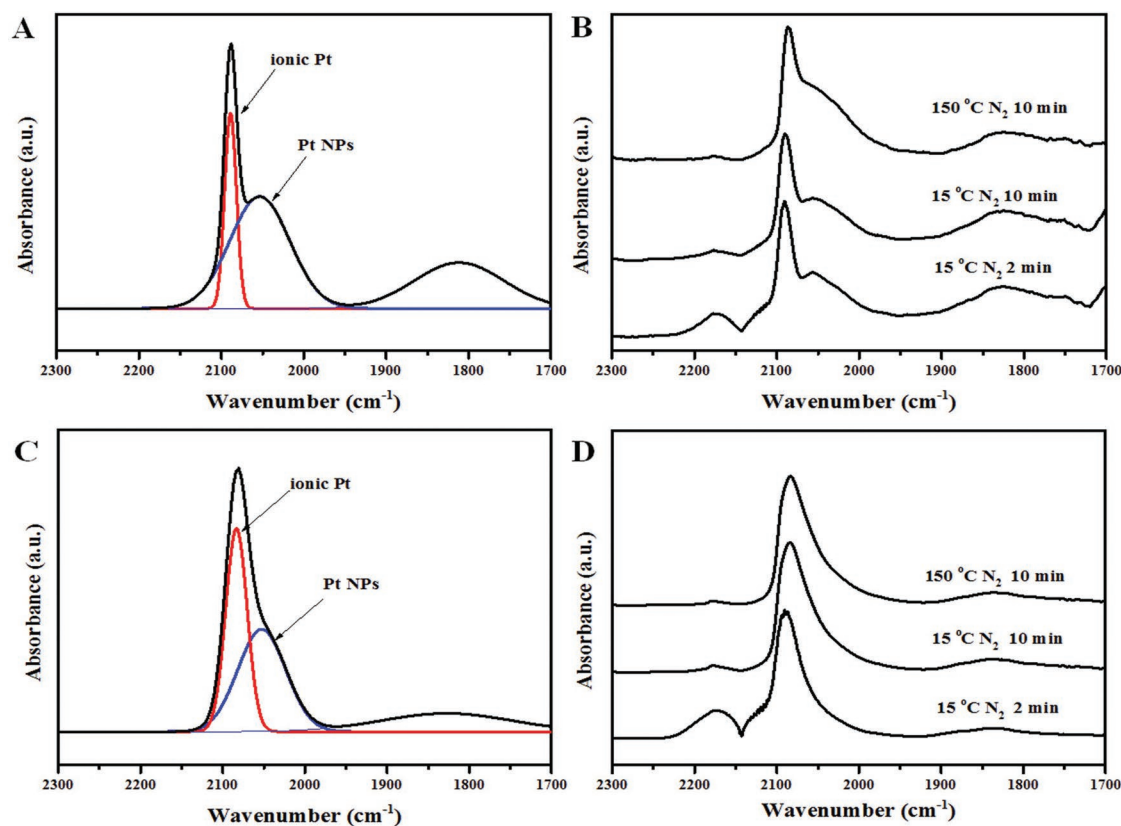


**Figure 6.** Selected DRIFT spectra of CO adsorbed on the ordered mesoporous A,B) Pt/Ce<sub>0.8</sub>Zr<sub>0.2</sub>O<sub>2</sub> and C,D) Pt/CeO<sub>2</sub> under different conditions. A,C) Adsorption of CO for 30 min; B,D) desorption with flushing in N<sub>2</sub> at different temperatures for different times.

lattice oxygen in CeO<sub>2</sub> and the reduced ceria is subsequently reoxidized by gas-phase oxygen.<sup>[1,2a,27]</sup> However, in our work the surface chemisorbed oxygen species with facile mobility and activity in mesoporous Pt/Ce<sub>0.8</sub>Zr<sub>0.2</sub>O<sub>2</sub> play a key role in enhancing the catalytic performance for CO oxidation, and thus the reaction mechanism can be interpreted as follows. First, the strong interaction between Ce<sub>0.8</sub>Zr<sub>0.2</sub>O<sub>2</sub> matrix and Pt species facilitates the formation of metallic Pt nanoparticles at the interface, where active CO molecules are selectively adsorbed and the chemisorbed oxygen species can be easily spilled over to neighboring Pt. Second, due to the lattice distortion and production of surface defect sites caused by zirconium doping, the surface oxygen mobility can be significantly enhanced, which facilitates the formation of surface oxygen vacancies and plays a pivotal role in enhancing the catalytic activity for CO oxidation. Third, the intrinsic porous structures with interconnected large pores and high surface areas of mesoporous Pt/Ce<sub>0.8</sub>Zr<sub>0.2</sub>O<sub>2</sub> provide abundant anchoring sites for Pt nanoparticles and numerous catalytically active interfaces within the mesostructure framework compared with the mesoporous Pt/Ce<sub>0.8</sub>Zr<sub>0.2</sub>O<sub>2</sub>-s.

In order to test and verify this mechanism, an additional ignition/extinction experiment was conducted to compare the catalysis hysteresis behavior of various catalysts in CO oxidation. The different catalytic activity during the light-off and light-out procedures was defined as the catalysis hysteresis behavior, which was usually found on Pt/Al<sub>2</sub>O<sub>3</sub> catalysts with a narrow hysteresis loop ( $\Delta T$ ) in previous reports.<sup>[33–35]</sup> Interestingly, our

mesoporous Pt/Ce<sub>0.8</sub>Zr<sub>0.2</sub>O<sub>2</sub> shows more visible catalysis hysteresis phenomenon in CO oxidation, presenting a much lower  $T_{100}$  value of 90 °C and a broader hysteresis loop ( $\Delta T = 40$  °C) during the extinction process (Figure 7A; Table S5, Supporting Information). However, the mesoporous Pt/Al<sub>2</sub>O<sub>3</sub>, Pt/ZrO<sub>2</sub>, and Pt/TiO<sub>2</sub> catalysts show higher light-off and light-out temperatures as well as narrower hysteresis loops than mesoporous Pt/CeO<sub>2</sub> and Pt/Ce<sub>0.8</sub>Zr<sub>0.2</sub>O<sub>2</sub>, indicating their superior catalytic activity and enhanced catalysis hysteresis (ECH) behavior for CO oxidation. To the best of our knowledge, few reports have been focused on this ECH phenomenon; even the normal or inverse hysteresis in CO oxidation was studied on Pt/Al<sub>2</sub>O<sub>3</sub> catalysts,<sup>[33–35]</sup> which was usually explained as a combination of three possible reasons, such as inherent kinetic bistability, interaction between reaction kinetics and diffusion phenomena, and locally high temperatures on the catalyst surface. The intrinsic surface properties of mesoporous Ce<sub>0.8</sub>Zr<sub>0.2</sub>O<sub>2</sub> solid solutions and interfacial interactions with Pt nanoparticles are quite different from the matrices of mesoporous Al<sub>2</sub>O<sub>3</sub>, ZrO<sub>2</sub>, TiO<sub>2</sub>, and CeO<sub>2</sub>. On one hand, CO adsorption on both metallic and cationic Pt species is favored at low temperatures, resulting in the predominant covering and self-poisoning of Pt surface by CO and quite low probability of oxygen species adsorbed on Pt surface. Therefore, a high temperature is needed to remove some weakly adsorbed CO molecules, evidenced by the gradual decrease of CO covered on metallic Pt sites (Figure 6B). Simultaneously, the chemisorbed oxygen species are quickly spilled

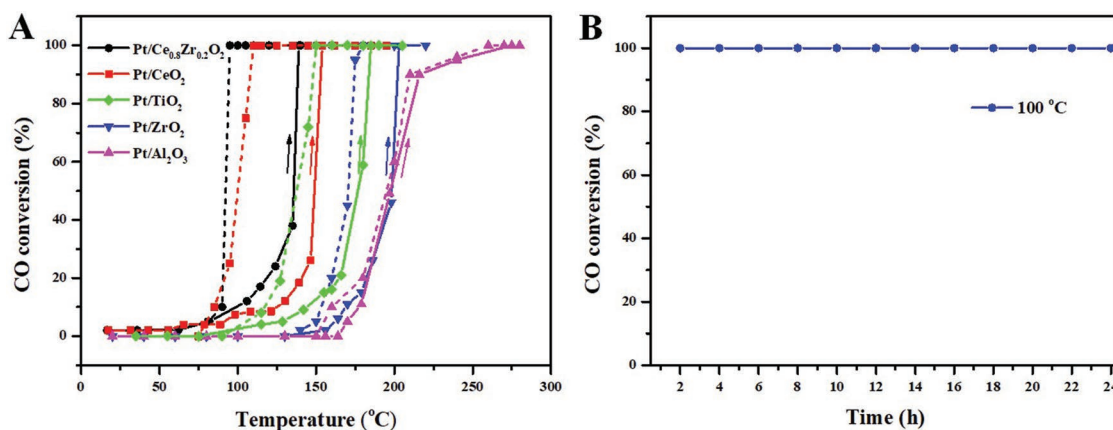


**Figure 7.** A) CO oxidation light-off (solid lines, indicated by arrows) and light-out (dotted lines) over different catalysts with large ordered mesopores. B) Successive evaluation of the ordered mesoporous Pt/Ce<sub>0.8</sub>Zr<sub>0.2</sub>O<sub>2</sub> catalyst for CO oxidation maintained at 100 °C for 24 h in the extinction stage. [CO] = 1 vol%, [O<sub>2</sub>] = 21 vol%, and balanced with N<sub>2</sub> (78 vol%) at a gas hourly space velocity of 60 000 mL g<sup>-1</sup> h<sup>-1</sup>. Temperature ramp: 1 °C min<sup>-1</sup>; pressure: 1 atm.

over to the vacant Pt sites in competition with CO, and react with the surface-adsorbed CO to form CO<sub>2</sub>.<sup>[36]</sup> On the other hand, as discussed in O 1s XPS analysis (Figure 5), both zirconium doping and platinum loading can promote the formation of chemisorbed oxygen adspecies and a high density of defect sites, which are shown to accelerate the diffusion and mobility of surface oxygen at the interface between Pt and Ce<sub>0.8</sub>Zr<sub>0.2</sub>O<sub>2</sub>. Once the reaction occurs, the active oxygen species are strongly adsorbed on Pt surface even at the decreased reaction temperature, which can be continuously supplied by the Ce<sub>0.8</sub>Zr<sub>0.2</sub>O<sub>2</sub> solid solution matrix, resulting in the lowered light-out temperature of 90 °C during the extinction process and the ECH phenomenon with  $\Delta T = 40$  °C. The XPS results of mesoporous Pt/Ce<sub>0.8</sub>Zr<sub>0.2</sub>O<sub>2</sub>-a after the stability test show that the O<sup>α</sup>/(O<sup>α</sup> + O<sup>β</sup>) ratio was decreased from 0.32 to 0.22 and the ratio of Pt<sup>2+</sup>/Pt<sup>0</sup> was increased from 0.29 to 0.35. These results imply that the surface chemisorbed oxygen species can immigrate from the mesoporous Ce<sub>0.8</sub>Zr<sub>0.2</sub>O<sub>2</sub> matrix to the immobilized Pt species and react with CO adsorbed in Pt nanoparticles' surface. Notably, the catalytic activity of mesoporous Pt/Ce<sub>0.8</sub>Zr<sub>0.2</sub>O<sub>2</sub> can be maintained at 100 °C over 24 h in the extinction stage (Figure 7B), suggesting that the high mobility of oxygen adspecies endows the catalyst with a high reaction rate and long stability. Mesoporous Pt/CeO<sub>2</sub> has a comparable ECH behavior ( $\Delta T = 40$  °C) but higher light-out temperature (110 °C), mainly due to the combined effects of facile formation and low mobility of surface chemisorbed oxygen species (Figure 5F). It should be mentioned that the effect of reaction exothermicity has been considered as the reason of catalysis hysteresis, which can result in the local overheating of catalyst surface. In order to prohibit the local overheating, a comparison test was conducted to dilute the catalyst of mesoporous Pt/Ce<sub>0.8</sub>Zr<sub>0.2</sub>O<sub>2</sub> with the same volume of quartz sands, and the same ECH behavior was also observed with  $\Delta T = 40$  °C, which is much broader than those in mesoporous Pt/Al<sub>2</sub>O<sub>3</sub>, Pt/ZrO<sub>2</sub>, and Pt/TiO<sub>2</sub> catalysts ( $\Delta T = 15, 23,$  and  $20$  °C, respectively) under the same light-out conditions, further proving that the ECH behavior is mainly due to the combination effects of reaction exothermicity and high mobility of oxygen adspecies of the Pt/Ce<sub>0.8</sub>Zr<sub>0.2</sub>O<sub>2</sub> and Pt/CeO<sub>2</sub> catalysts.

### 3. Conclusion

In summary, highly ordered mesoporous Ce<sub>x</sub>Zr<sub>1-x</sub>O<sub>2</sub> (0 < x < 1) solid solutions with high surface area, large pore size, crystalline walls, and surface reducibility have been rationally and conveniently synthesized through a solvent evaporation-induced co-assembly process by using PEO-*b*-PS diblock copolymer as a template, and Zr(acac)<sub>4</sub> and CeCl<sub>3</sub>·7H<sub>2</sub>O as the inorganic source. By employing the obtained mesoporous Ce<sub>x</sub>Zr<sub>1-x</sub>O<sub>2</sub> solid solutions as a support, ultrafine Pt nanoparticles (about 4.0 nm) were in situ confined inside the mesopores without pore blocking, forming the mesoporous composite nanocatalysts with highly dispersed Pt species for CO catalytic oxidation at very low temperatures. Compared with other mesoporous Pt/Ce<sub>x</sub>Zr<sub>1-x</sub>O<sub>2</sub> materials and the mesoporous Pt/Ce<sub>0.8</sub>Zr<sub>0.2</sub>O<sub>2</sub>-s with small pore size, the large-pore mesoporous Pt/Ce<sub>0.8</sub>Zr<sub>0.2</sub>O<sub>2</sub> catalyst shows superior catalytic performance with T<sub>100</sub> value of 130 °C and long-term catalytic stability over 50 cycles. The detailed investigation results of H<sub>2</sub>-TPR, XPS, in situ CO DRIFTS, and the light-out experiments revealed that its outstanding CO oxidation behavior is mainly attributed to the synergistic interface effect between Pt nanoparticles and the highly interconnected large-pore structures of mesoporous Pt/Ce<sub>0.8</sub>Zr<sub>0.2</sub>O<sub>2</sub> catalyst. The lattice distortion and formation of rich surface defect sites induced by zirconium doping were found to be responsible for the increased surface oxygen mobility that facilitates the formation of surface oxygen vacancies and enhances the catalytic activity for CO oxidation. Apart from the Ce<sub>0.8</sub>Zr<sub>0.2</sub>O<sub>2</sub> support, the highly dispersed and accessible metallic Pt nanoparticles within the mesoporous Ce<sub>0.8</sub>Zr<sub>0.2</sub>O<sub>2</sub> matrix provide abundant active sites for CO adsorption and oxidation, which can also enhance the catalytic efficiency and thermal stability. Considering their facile synthesis and excellent catalytic performance, the ordered mesoporous Pt/Ce<sub>x</sub>Zr<sub>1-x</sub>O<sub>2</sub> materials hold a great promise as the high-efficiency catalysts for vehicle emission abatement and other complex heterogeneous catalysis.

### Supporting Information

Supporting Information is available from the Wiley Online Library or from the author.

## Acknowledgements

This work was supported by the NSF of China (51372041, 21673048, 51822202, and 51772050), Key Basic Research Program of Science and Technology Commission of Shanghai Municipality (17JC1400100), Sponsored by Program of Shanghai Academic Research Leader (19XD1420300), Youth Top-Notch Talent Support Program of China, Shanghai Rising-Star Program (18QA1400100), and DHU Distinguished Young Professor Program.

## Conflict of Interest

The authors declare no conflict of interest.

## Keywords

catalysis hysteresis, CeO<sub>2</sub>-ZrO<sub>2</sub> solid solutions, co-assembly, CO oxidation, mesoporous materials

Received: June 12, 2019

Revised: July 12, 2019

Published online:

- [1] L. Nie, D. Mei, H. Xiong, B. Peng, Z. Ren, X. Hernandez, A. Delariva, M. Wang, M. H. Engelhard, L. Kovarik, *Science* **2017**, 358, 1419.
- [2] a) J. Lee, Y. Ryou, X. Chan, T. J. Kim, D. H. Kim, *J. Phys. Chem. C* **2016**, 120, 25870; b) K. Ding, A. Gulec, A. M. Johnson, N. M. Schweitzer, G. D. Stucky, L. D. Marks, P. C. Stair, *Science* **2015**, 350, 189; c) S. Gatla, D. Aubert, G. Agostini, O. Mathon, S. Pascarelli, T. Lunkenbein, M. G. Willinger, H. Kaper, *ACS Catal.* **2016**, 6, 6151; d) J. Jones, H. Xiong, A. T. Delariva, E. J. Peterson, H. Pham, S. R. Challa, G. Qi, S. Oh, M. H. Wiebenga, X. I. Pereira Hernández, *Science* **2016**, 353, 150.
- [3] a) N. Zhang, Y. J. Xu, *Chem. Mater.* **2013**, 25, 1979; b) L. Adijanto, D. A. Bennett, C. Chen, A. S. Yu, M. Cargnello, P. Fornasiero, R. J. Gorte, J. M. Vohs, *Nano Lett.* **2013**, 13, 2252; c) P. Lu, C. T. Campbell, Y. Xia, *Nano Lett.* **2013**, 13, 4957.
- [4] L. Li, G. Wu, B.-Q. Xu, *Carbon* **2006**, 44, 2973.
- [5] K. An, S. Alayoglu, N. Musselwhite, S. Plamthottam, G. Melaeat, A. E. Lindeman, G. A. Somorjai, *J. Am. Chem. Soc.* **2013**, 135, 16689.
- [6] Y. Zhou, D. E. Doronkin, M. Chen, S. Wei, J.-D. Grunwaldt, *ACS Catal.* **2016**, 6, 7799.
- [7] a) X. Xu, Q. Fu, L. Gan, J. Zhu, X. Bao, *J. Phys. Chem. B* **2018**, 122, 984; b) X. Yang, X. Cheng, A. Elzatahry, J. Chen, A. Alghamdi, Y. Deng, *Chin. Chem. Lett.* **2019**, 30, 324.
- [8] D. Gu, J. C. Tseng, C. Weidenthaler, H. J. Bongard, B. Spliethoff, W. Schmidt, F. Soulamani, B. M. Weckhuysen, F. Schuth, *J. Am. Chem. Soc.* **2016**, 138, 9572.
- [9] a) Y. Cheng, W. Song, J. Liu, H. Zhang, Z. Zhao, C. Xu, Y. Wei, E. J. M. Hensen, *ACS Catal.* **2017**, 7, 3883; b) J. Serrano-Ruiz, J. Luettich, A. Sepulveda-Escribano, F. Rodriguez-Reinoso, *J. Catal.* **2006**, 241, 45; c) C. M. Yeung, K. M. Yu, Q. J. Fu, D. Thompsett, M. I. Petch, S. C. Tsang, *J. Am. Chem. Soc.* **2005**, 127, 18010; d) G. N. Vayssilov, Y. Lykhach, A. Migani, T. Staudt, G. P. Petrova, N. Tsud, T. Skala, A. Bruix, F. Illas, K. C. Prince, V. Matolin, K. M. Neyman, J. Libuda, *Nat. Mater.* **2011**, 10, 310.
- [10] a) H. Arandiyani, H. Dai, K. Ji, H. Sun, J. Li, *ACS Catal.* **2015**, 5, 1781; b) A. M. Hernández-Giménez, L. P. dos Santos Xavier, A. Bueno-López, *Appl. Catal., A* **2013**, 462–463, 100; c) S. Ricote, G. Jacobs, M. Milling, *Appl. Catal., A* **2006**, 303, 35.
- [11] G. Zhang, Z. Zhao, J. Liu, G. Jiang, A. Duan, J. Zheng, S. Chen, R. Zhou, *Chem. Commun.* **2010**, 46, 457.
- [12] a) H. A. Aleksandrov, K. M. Neyman, K. I. Konstantin, G. N. Vayssilov, *Phys. Chem. Chem. Phys.* **2016**, 18, 22108; b) G. Zhang, Z. Zhao, J. Xu, J. Zheng, J. Liu, G. Jiang, A. Duan, H. He, *Appl. Catal., B* **2011**, 107, 302.
- [13] L. Katta, P. Sudarsanam, G. Thirumurthulu, B. M. Reddy, *Appl. Catal., B* **2010**, 101, 101.
- [14] a) C. Wang, X.-K. Gu, H. Yan, Y. Lin, J. Li, D. Liu, W.-X. Li, J. Lu, *ACS Catal.* **2017**, 7, 887; b) R. Kopelent, J. A. van Bokhoven, J. Szlachetko, J. Edebeli, C. Paun, M. Nachtegaal, O. V. Safonova, *Angew. Chem., Int. Ed.* **2015**, 54, 8728.
- [15] a) Q. Wang, B. Zhao, G. Li, R. Zhou, *Environ. Sci. Technol.* **2010**, 44, 3870; b) J. Ge, X. Yang, J. Luo, J. Ma, Y. Zou, J. Li, W. Luo, X. Cheng, Y. Deng, *Appl. Mater. Today* **2019**, 15, 482.
- [16] a) W. Li, J. Liu, D. Zhao, *Nat. Rev. Mater.* **2016**, 1; b) J. Wang, J. Tang, B. Ding, V. Malgras, Z. Chang, X. Hao, Y. Wang, H. Dou, X. Zhang, Y. Yamauchi, *Nat. Commun.* **2017**, 8, 15717; c) M. Pramanik, S. Tominaka, Z. Wang, T. Takei, Y. Yamauchi, *Angew. Chem., Int. Ed.* **2017**, 56, 13508; d) B. Jiang, C. Li, Ö. Dag, H. Abe, T. Takei, T. Imai, M. Hossain, M. Islam, K. Wood, J. Henzie, Y. Yamauchi, *Nat. Commun.* **2017**, 8, 15581; e) J. Hwang, S. Kim, U. Wiesner, J. Lee, *Adv. Mater.* **2018**, 30, 1801127; f) M. Kim, E. Lim, S. Kim, C. Jo, J. Chun, J. Lee, *Adv. Funct. Mater.* **2017**, 27, 1603921; g) C. Jo, J. Hwang, W. Lim, J. Lim, K. Hur, J. Lee, *Adv. Mater.* **2018**, 30, 1703829; h) X. Wang, L. Bai, H. Liu, X. Yu, Y. Yin, C. Gao, *Adv. Funct. Mater.* **2018**, 28, 1704208; i) J. Joo, I. Lee, M. Dahl, G. Moon, F. Zaera, Y. Yin, *Adv. Funct. Mater.* **2013**, 23, 4246; j) T. Huang, W. Chang, J. Chien, C. Kang, P. Yang, M. Chen, J. He, *J. Mater. Chem. C* **2013**, 1, 7593; k) H. Wang, J. He, *Adv. Energy Mater.* **2017**, 7, 1602385; l) X. Zhou, X. Cheng, Y. Zhu, A. Elzatahry, A. Alghamdi, Y. Deng, D. Zhao, *Chin. Chem. Lett.* **2018**, 29, 405; m) Y. Ren, X. Yang, X. Zhou, W. Luo, Y. Zhang, X. Cheng, Y. Deng, *Chin. Chem. Lett.* **2019**, <https://doi.org/10.1016/j.ccllet.2019.01.019>.
- [17] C. Ho, J. C. Yu, X. Wang, S. Lai, Y. Qiu, *J. Mater. Chem.* **2005**, 15, 2193.
- [18] E. L. Crepaldi, G. J. A. A. Soler-Illia, A. Bouchara, D. Grosso, D. Durand, C. Sanchez, *Angew. Chem., Int. Ed.* **2003**, 42, 347.
- [19] Q. Yuan, Q. Liu, W.-G. Song, W. Feng, W.-L. Pu, L.-D. Sun, Y.-W. Zhang, C.-H. Yan, *J. Am. Chem. Soc.* **2007**, 129, 6698.
- [20] T. Brezesinski, M. Antonietti, M. Groenewolt, N. Pinna, B. Smarsly, *New J. Chem.* **2005**, 29, 237.
- [21] J. Zhang, Y. Deng, D. Gu, S. Wang, L. She, R. Che, Z.-S. Wang, B. Tu, S. Xie, D. Zhao, *Adv. Energy Mater.* **2011**, 1, 241.
- [22] a) Y. Li, W. Luo, N. Qin, J. Dong, J. Wei, W. Li, S. Feng, J. Chen, J. Xu, A. A. Elzatahry, M. H. Es-Saheb, Y. Deng, D. Zhao, *Angew. Chem., Int. Ed.* **2014**, 53, 9035; b) J. Ma, Y. Ren, X. Zhou, L. Liu, Y. Zhu, X. Cheng, P. Xu, X. Li, Y. Deng, D. Zhao, *Adv. Funct. Mater.* **2018**, 28, 1705268.
- [23] W. Luo, Y. Li, J. Dong, J. Wei, J. Xu, Y. Deng, D. Zhao, *Angew. Chem., Int. Ed.* **2013**, 52, 10505.
- [24] X. Yang, X. Cheng, H. Song, J. Ma, P. Pan, A. A. Elzatahry, J. Su, Y. Deng, *Adv. Healthcare Mater.* **2018**, 7, 1800149.
- [25] M. Fernández-García, X. Wang, C. Belver, A. Iglesias-Juez, J. C. Hanson, J. A. Rodriguez, *Chem. Mater.* **2005**, 17, 4181.
- [26] M. Yashima, K. Morimoto, N. Ishizawa, M. Yoshimura, *J. Am. Ceram. Soc.* **1993**, 76, 1745.
- [27] a) M. Mao, H. Lv, Y. Li, Y. Yang, M. Zeng, N. Li, X. Zhao, *ACS Catal.* **2016**, 6, 418; b) Y. Yan, H. Li, Z. Lu, X. Wang, R. Zhang, G. Feng, *Chin. Chem. Lett.* **2019**, 30, 1153.
- [28] a) Y. Chen, J. Gao, Z. Huang, M. Zhou, J. Chen, C. Li, Z. Ma, J. Chen, X. Tang, *Environ. Sci. Technol.* **2017**, 51, 7084; b) N. Li, Q. Chen, L. Luo, W. Huang, M. Luo, G. Hu, J. Lu, *Appl. Catal., B* **2013**, 142–143, 523.
- [29] X. Wu, J. Fan, R. Ran, D. Weng, *Chem. Eng. J.* **2005**, 109, 133.

- [30] a) L. Liu, F. Zhou, L. Wang, X. Qi, F. Shi, Y. Deng, *J. Catal.* **2010**, 274, 1; b) F. Zheng, S. Alayoglu, J. Guo, V. Pushkarev, Y. Li, P.-A. Glans, J.-l. Chen, G. Somorjai, *Nano Lett.* **2011**, 11, 847.
- [31] Y. Ji, D. Xu, S. Bai, U. Graham, M. Crocker, B. Chen, C. Shi, D. Harris, D. Scapens, J. Darab, *Ind. Eng. Chem. Res.* **2017**, 56, 111.
- [32] J. Neugeboren, D. Borodin, H. W. Hahn, J. Altschäffel, A. Kandratsenka, D. J. Auerbach, C. T. Campbell, D. Schwarzer, D. J. Harding, A. M. Wodtke, T. N. Kitsopoulos, *Nature* **2018**, 558, 280.
- [33] M. Casapu, A. Fischer, A. M. Gänzler, R. Popescu, M. Crone, D. Gerthsen, M. Türk, J. D. Grunwaldt, *ACS Catal.* **2017**, 7, 343.
- [34] A. Abedi, R. Hayes, M. Votsmeier, W. S. Epling, *Catal. Lett.* **2012**, 142, 930.
- [35] P. A. Carlsson, L. Österlund, P. Thormählen, A. Palmqvist, E. Fridell, J. Jansson, M. Skoglundh, *J. Catal.* **2004**, 226, 422.
- [36] W. Wang, J. Zhang, F. Wang, B. Mao, D. Zhan, Z. Tian, *J. Am. Chem. Soc.* **2016**, 138, 9057.